View Identification Assisted Fully Convolutional Network for Lung Field Segmentation of Frontal and Lateral Chest Radiographs

YUHUA XI[1,2,*], **LIMING ZHONG**[1,2,*], **WEIJIE XIE**[1,2], **GENGGENG QIN**[3], **YUNBI LIU**[1,2], **QIANJIN FENG**[1,2], (Member, IEEE), AND **WEI YANG**[1,2]

[1]School of Biomedical Engineering, Southern Medical University, Guangzhou 510515, China
[2]Guangdong Provincial Key Laboratory of Medical Image Processing, Guangzhou 510515, China
[3]Department of Radiology, Nanfang Hospital, Southern Medical University, Guangzhou 510515, China

Corresponding author: Wei Yang (weiyanggm@gmail.com)

*Yuhua Xi and Liming Zhong contributed equally to this work.

ABSTRACT Locating lung field is a critical and fundamental processing stage in the automated analysis of chest radiographs (CXRs) for pulmonary disorders. During the routine examination of CXRs, using both frontal and lateral CXRs can benefit clinical diagnosis of cardiothoracic and lung diseases. However, the accurate segmentation of lung fields on both frontal and lateral CXRs is still challenging due to the blurry boundary of the lung field on lateral CXRs and the poor generalization ability of the models. Existing deep learning-based methods focused on lung field segmentation on frontal CXRs, and the generalization ability of these methods on the different type of CXRs (e.g., pediatric CXRs) and new lung diseases (e.g., COVID-19) has not been tested. In this paper, a view identification assisted fully convolutional network (VI-FCN) is proposed for the segmentation of lung fields on frontal and lateral CXRs simultaneously. The VI-FCN consists of an FCN branch for lung field segmentation and a view identification branch for identification of the frontal and lateral CXRs and for enhancing the lung field segmentation. To improve the generalization ability of VI-FCN, six public datasets and our frontal and lateral CXRs (over 2000 CXRs) were collected for training. The segmentation of lung fields on the Japanese Society of Radiological Technology (JSRT) dataset yields mean dice similarity coefficient (DSC) of 0.979 ± 0.008, mean Jaccard index (Ω) of 0.959 ± 0.016, and mean boundary distance (MBD) of $1.023 \pm 0.487mm$. Besides, the VI-FCN achieves mean DSC of 0.973 ± 0.010, mean Ω of 0.947 ± 0.018, and mean MBD of $1.923 \pm 0.755mm$ for the segmentation of lung fields on our lateral CXRs. The experiments demonstrate the superior performance of the proposed VI-FCN over most of existing state-of-the-art methods. Moreover, the proposed VI-FCN achieves promising results on untrained pediatric CXRs and COVID-19 datasets.

INDEX TERMS Chest radiographs, lung field segmentation, generalization ability, COVID-19.

I. INTRODUCTION

Chest radiography (CXR) is one of the most affordable and frequently used medical imaging techniques, which has the advantages of easy accessibility, economy, removal, and low radiation dose in daily clinical routine compared to other imaging techniques [1]. In most areas and medical facilities, modern digital radiography machines are readily available. Frontal and lateral CXRs can benefit clinical diagnosis

The associate editor coordinating the review of this manuscript and approving it for publication was Amin Zehtabian.

of cardiothoracic and lung diseases. Generally, the use of both frontal and lateral CXRs can help radiologists determine diagnostic uncertainties, especially for a specific pulmonary opacity within the chest cavity. Automatic analysis of CXRs can assist in population screening, interpretation of abnormal cases, and controlling inter-reader variability across radiologists [2]. Lung field segmentation (as shown in Fig. 1) is a critical initial step for image-based pulmonary analysis [3], [4].

Since lung field segmentation for CXRs can benefit clinical diagnosis and automatic detection of abnormalities, a great
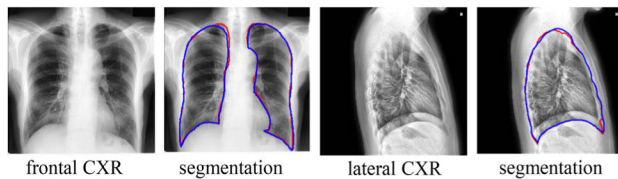
FIGURE 1. Examples of lung field segmentation. The first and third columns are frontal and lateral CXRs, respectively. The rest of columns are lung field segmentation. Blue and red contours indicate the ground truth and automatic segmentation results, respectively.

deal of literature has been proposed for lung field segmentation. The mainstream lung field segmentation methods can be grouped into two categories: classic-based approaches and deep learning-based approaches.

Classic-based approaches, including rule-based methods [4]–[6], pixel classification-based methods [7], [8], deformable shape-based methods [9-11], and hybrid methods [12-15], have different focuses and advantages. Rule-based methods [4-6], which use predefined knowledge about the lung field to create a set of rules, are usually used as initial segmentation algorithms. Although a set of simple operations, such as thresholding, morphological operations, and connected component analysis, are added in rule-based methods, they still cannot resolve the cascaded accumulation of errors. Pixel classification-based methods [7], [8] learn the probability of each pixel of being a lung or a non-lung pixel using a classifier. The drawback of pixel classification-based methods is the lack of model constraints on the boundary of lung fields. To address this problem, deformable shape-based methods [9], [10], [16] use the priors of low level appearance and shape to define the lung fields. The earliest deformable shape-based algorithms are the active shape model (ASM) [17] and the active appearance model (AAM) [18]. Typically, compared to the ASM and AAM, scale-invariant feature transforms [11], shape particle filtering [16], and global edge and region forces [19] have demonstrated superior performance through extracting low level localized appearance features and high level global features. To further improve the performance of lung field segmentation, hybrid methods [12-15] combine the best parts of pixel classification and deformable shape to refine the detection of the lung boundary. Peng *et al*. [20] proposed a hybrid semi-automatic method called Hull-Closed Polygonal Line Method (Hull-CPLM) to detect the boundaries of the lung region of interest. Recently, Peng *et al*. [21] also developed a model called DBN-DLP consisting of preprocessing subnetwork and refinement subnetwork. However, the major drawbacks of classic-based approaches include long consuming time and modest accuracy of lung field segmentation.

The superior performance and less execution time for lung field segmentation of deep learning-based methods have been demonstrated as compared to classic-based approaches. Deep learning-based methods treat lung segmentation as a pixel classification problem and handle it by training

and optimizing convolutional neural networks (CNNs) with paired data (CXR and its corresponding mask). Among them, graph convolution networks [22] and multimodal [23] deep learning have been proposed for image classification. Despite the superior performance of deep learning-based methods, only a few studies have been reported for lung field segmentation on CXRs [24]. Existing deep learning-based methods [25-32] use encoder-decoder convolutional neural networks (Encoder-Decoder CNN) [25], U-Net [26], [27], the improved U-net [28], fully convolutional network (FCN) [29], [30], Deeplabv3+ [31], and structure correcting adversarial network (SCAN) [32] to accurately segment the lung fields. However, these methods mainly focus on the segmentation of frontal CXRs, and evaluate the model on Japanese Society of Radiological Technology (JSRT) [33] dataset or their own dataset. Moreover, the generalization ability of these methods on the different type of CXRs (e.g., pediatric CXRs) and new lung disease (e.g., COVID-19) has not been tested. It is different from above methods that we present a multi-task network architecture named VI-FCN. Our VI-FCN can achieve lung field segmentation and view identification of frontal and lateral CXRs, simultaneously. Moreover, the proposed VI-FCN achieves promising results in two testing datasets (e.g., pediatric and COVID-19 CXRs).

Under the global pandemic of COVID-19, developing a model for lung field segmentation to analyze CXRs for COVID-19 diagnosis is important. However, due to the emergent attributes of the COVID-19, it has been difficult to collect large amounts of COVID-19 CXRs for training a new model. Oh *et al*. [34] used FC-DenseNet 103 [35] to train a model using two public datasets for lung field segmentation to further analyze the diagnosis of COVID-19. Yeh *et al*. [36] used a U-Net [26] framework to train a simple segmentation model on two public datasets for lung field segmentation as a basic step of COVID-19 screening. As in [34], [36], the segmentation of lung fields is a key step in the training of a classification model. Although the promising lung field segmentation of frontal CXRs for COVID-19 has been achieved, the results of lung field segmentation evaluated on public datasets are not optimal. Moreover, only the frontal CXRs were added in the analysis. Adding both frontal and lateral CXRs can make the clinical diagnosis of COVID-19 more effective. Due to the poor generalization ability of the model, false labels occur in the lung field segmentation for COVID-19 CXRs.

According to the aforementioned methods, lung field segmentation suffers from the following challenges:

1) Due to the blurry boundaries of lateral CXRs caused by an overlapping left lung and right lung, an overlapping left lung and heart, and an overlapping thoracic vertebra and the boundary of lungs, few studies had attempted to segment lung fields on lateral CXRs, and barely no studies had attempted to simultaneously segment lung fields on lateral and frontal CXRs (As shown in Fig. 2 (a)).
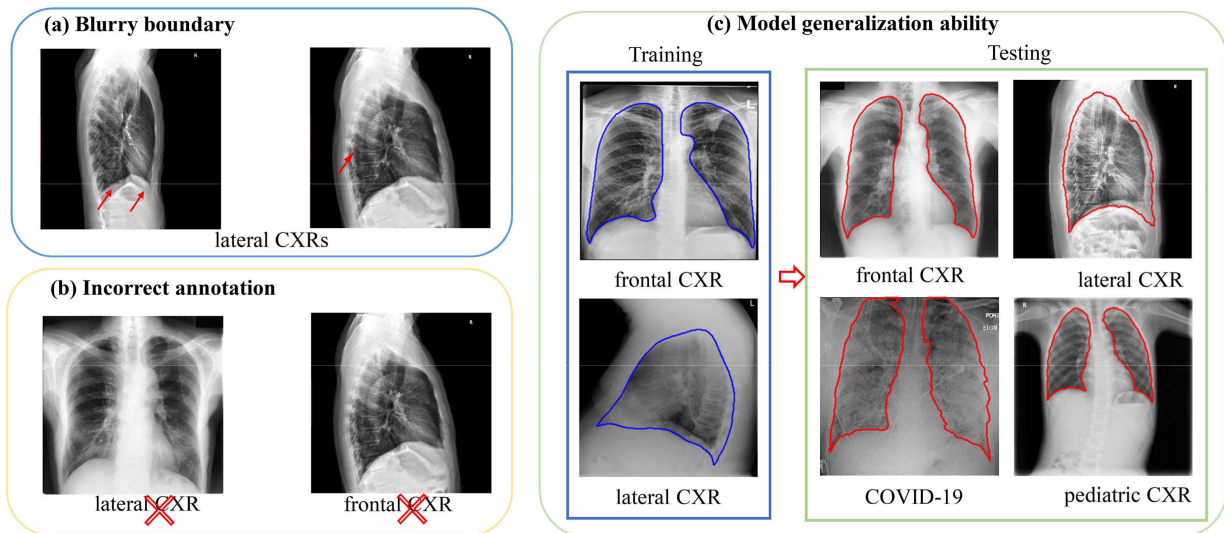
FIGURE 2. The challenges of lung field segmentation including (a) the blurry boundary in lateral CXRs, (b) incorrect annotation, and (c) the generalization ability of model.

2) There may be incorrect annotations on frontal CXRs and lateral CXRs in DICOM images (as shown in Fig. 2 (b)). The classification result of frontal CXRs and lateral CXRs is important for correcting the incorrect annotations and improving the performance of lung field segmentation.

3) Existing learning-based methods are trained using limited data and evaluated on JSRT dataset or their own data, the generalization ability of these methods has not been tested (as shown in Fig. 2 (c)).

To solve the aforementioned drawbacks, we proposed a view identification assisted fully convolutional network named VI-FCN, as shown in Fig. 3, for lung field segmentation of frontal CXRs and lateral CXRs simultaneously. The VI-FCN consists of two branches including an FCN for the lung field segmentation of frontal CXRs and lateral CXRs and a view identification (VI) for the classification of frontal CXRs and lateral CXRs. The developed VI-FCN can overcome the challenges of 1) and 2) by achieving the lung field segmentation and classification on frontal CXRs and lateral CXRs within a single model with arbitrary input. In order to overcome the challenges of 3), large amounts of public data and our own data, which are from different centers and different conditions, were collected to train the proposed VI-FCN. Two datasets not included in the training (including pediatric CXRs and COVID-19 CXRs) were used to intuitively show the generalization ability of the proposed VI-FCN. The package for VI-FCN, along with its documentation, is freely accessible from the website **https://github.com/SMU-MedicalVision/VI-FCN**.

The proposed VI-FCN framework has the following three contributions:

1) To the best of our knowledge, few studies had attempted to simultaneously segment the lung fields on lateral and frontal CXRs. The proposed VI-FCN can simultaneously segment the lung fields on lateral and frontal CXRs in one single model.

2) The VI branch in VI-FCN can assist in improving the performance of lung field segmentation and correct the incorrect annotations of frontal CXRs and lateral CXRs in DICOM images.

3) The proposed VI-FCN can improve the poor generalization ability of model by using large amounts of data from different centers and different conditions. The performance of VI-FCN was evaluated on two the untrained datasets (pediatric CXRs and COVID-19 CXRs)). The experimental results demonstrate the superior performance of the proposed VI-FCN.

This paper is organized as follows: section 2 presents our proposed VI-FCN method, section 3 presents the experimental setup, section 4 presents the experimental results, and sections 5-6 present the discussion and conclusion, respectively. Finally, we describe the details of the network architecture in appendix section.

II. METHOD

In this study, a VI-FCN, as shown in Fig. 3, for multi-application image analysis is proposed to tackle lung field segmentation and view identification in frontal and lateral CXRs, and it consists of two paths. (1) In the segmentation path, an FCN framework [35] is employed to complete the simultaneous segmentation of the lung field on lateral and frontal CXRs, which is particularly effective and efficient in detecting lung regions. (2) In the auxiliary path for view identification, the downsampling path of segmentation task is shared, and the features extracted from the shared path are fed into a classifier to obtain a view identification result.
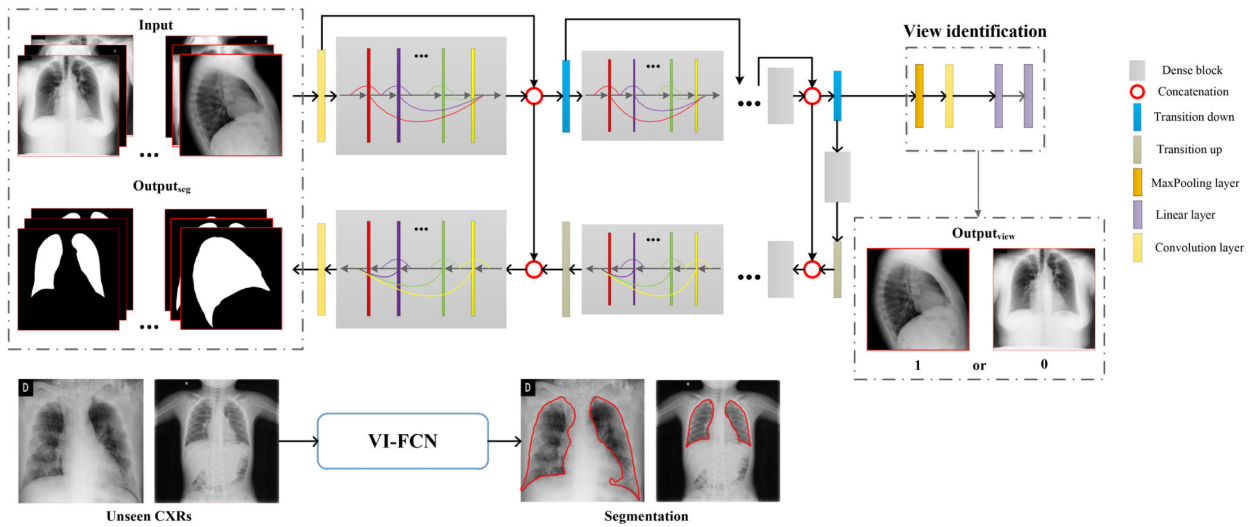
FIGURE 3. The framework of the proposed VI-FCN which includes FCN for lung field segmentation of frontal CXRs and lateral CXRs and VI for classification of frontal CXR and lateral CXR.

A. MATHEMATICAL FORMULATION

The multiple target estimations of the CXR images can be summarized as a multi-output classification problem. Given a training dataset $T = \{x_i, y_i\}_{i=1}^{N} \cup \{x_j, y_j\}_{j=1}^{M}$, our goal is to train a multi-output classification model (i.e., the VI-FCN) to learn a mapping f:

$$f : x \in \mathbb{R}^{d \times d} \rightarrow y \in \mathbb{R}^{d \times d} \oplus \mathbb{R} \quad (1)$$

where x_i/x_j and y_i/y_j denote the frontal/lateral CXR image and the corresponding multiple task outputs, and N and M are the number of frontal and lateral CXRs training samples, respectively. $\mathbb{R}^{d \times d}$ represents an image matrix and $\mathbb{R}$ is real number. The VI-FCN model aims to learn a reliable pixel classifier and a view identification module simultaneously.

B. THE VI-FCN MODEL FOR LUNG FIELD SEGMENTATION AND VIEW IDENTIFICATION

The proposed VI-FCN is employed to simultaneously predict lung field segmentation and view identification in frontal and lateral CXRs. The objective function can be formulated as:

$$\widetilde{\Theta} = \underset{\Theta}{\arg\min}\, C(\Theta_{seg}, \Theta_{VI}) \quad (2)$$

$$C(\Theta_{seg}, \Theta_{VI}) = L(\Theta_{seg}) + \lambda L(\Theta_{VI}) \quad (3)$$

where $L(\Theta_{seg})$ denotes the loss of lung field segmentation task, $L(\Theta_{VI})$ denotes the loss of view identification task, and Θ represents the trainable parameters through the network. Since the prediction of the view classification is an auxiliary task in our multi-task network, a tuning parameter λ is assigned for the optimization of the network. And λ is set in order to allow relative weighting of the individual components of the total loss function.

In our work, a sigmoid function with cross entropy loss function was used to optimize both the tasks of segmentation and view identification, which guarantees numerical

stability. $L(\Theta_{seg})$ and $L(\Theta_{VI})$ for binary prediction can be formulated as:

$$L(\Theta_{seg}) = -y_{true}^{s} \log(\delta(y_{pre}^{s})) + (1 - y_{true}^{s}) \log(1 - \delta(y_{pre}^{s})) \quad (4)$$

$$L(\Theta_{VI}) = -y_{true}^{v} \log(\delta(y_{pre}^{v})) + (1 - y_{true}^{v}) \log(1 - \delta(y_{pre}^{v})) \quad (5)$$

where y_{true}^{s} and $y_{true}^{v} \in \{0, 1\}$ denote the ground truths, y_{pre}^{s} and y_{pre}^{v} specify the predicted probabilities of two tasks. Sigmoid function $\delta(z)$ is defined as:

$$\delta(z) = \frac{1}{1 + e^{-z}} \quad (6)$$

The parameters Θ were trained through our proposed VI-FCN. As for the task of lung field segmentation, FC-DenseNet [35] was used as the backbone of VI-FCN. The segmentation path comprises 11 dense blocks, 5 transition down (TD) layers and 5 transition up (TU) layers. In dense block, the skip connections between the interior layers contribute to strengthening the feature propagations along the network and encourage feature reuse. Let x_l be the output of the lth layer. The output of the lth layer is defined as $x_l = H([x_{l-1}, x_{l-2}, \ldots, x_0])$, where [.] represents the concatenation operation, and H represents a series of operations composed of batch normalization (BN) [37], followed by a rectified linear unit (ReLU) [38], a convolution layer with a 3×3 kernel size and a stride of 1 without reducing the resolution of feature maps, and the rate of dropout is 0.2. After the downsampling path, a dense block is attached at the 'bottom' of our network architecture to further process the high level features obtained by the downsampling path. The pre-processed frontal or lateral CXR is randomly fed into the VI-FCN to predict the lung field on the segmentation path. The classification of whether the input image is a frontal CXR or a lateral CXR and an accurate lung field segmentation can be obtained in a single model.

TABLE 1. The detailed summary of all datasets.

Dataset	Device	Pathology	Quantity
CRASS	DR (Delft)	TB	Frontal (299)
MC	CR (Eureka)	TB	Frontal (138)
TB	CR (KODAK)	TB	Frontal (106)
Shenzhen	DR (Philips)	TB	Frontal (566)
OpenIST	-	-	Frontal (275)
JSRT	scanned film	nodule	Frontal (247)
COVID-19	-	coronavirus	Frontal (161)
			Lateral (13)
Ours (adult)	DR (GE)	-	Frontal (190)
			Lateral (452)
Ours (pediatric)	DR (GE)	-	Frontal (260)

As for the task of view identification, a classifier module is added by following the output of downsampling path. The classifier module is composed of a maxpooling layer, followed by ReLU, and fully connected layers. The classifier module can accurately determine whether the input belongs to the frontal CXR or lateral CXR.

III. EXPERIMENTAL SETUP

A. DATASETS
The datasets used for training and testing were collected from six public frontal CXR datasets and our frontal and lateral CXR datasets. The six public frontal CXR datasets include the Chest Radiograph Anatomical Structure Segmentation (CRASS) dataset,[1] the Montgomery County (MC) dataset,[2] the Belarus tuberculosis (TB) dataset,[3] the third People's Hospital of Shenzhen, China (Shenzhen) dataset,[4] OpenIST dataset,[5] and Japanese Society of Radiological Technology (JSRT) dataset.[6,7]

Our frontal and lateral CXR dataset was collected retrospectively from Nanfang Hospital, Southern Medical University, Guangzhou, China. All the CXRs were acquired on Discovery XR656, GE Healthcare. All the CXRs were restored in anonymized DICOM files with a 14-bit depth. The mean of manually delineated masks by three radiologists were used as ground true masks.

Due to the global pandemic of COVID-19, medical resources have been insufficient in many regions. Two datasets, including the pediatric CXRs and COVID-19 CXRs without ground true masks, were directly used for evaluating the generalization ability of the proposed VI-FCN model. Specifically, the pediatric CXRs were collected retrospectively from Zhujiang Hospital, Southern Medical University, Guangzhou, China. The detailed summary of all datasets is listed in Table 1.

[1] http://crass.grand-challenge.org/
[2] http://openi.nlm.nih.gov/imgs/collections/NLM-MontgomeryCXRSet.zip
[3] http://tuberculosis.by/?page_id=20
[4] http://openi.nlm.nih.gov/imgs/collections/ChinaSet_AllFiles.zip
[5] https://github.com/pi-null-mezon/OpenIST
[6] http://www.isi.uu.nl/Research/Databases/SCR/
[7] https://github.com/ieee8023/covid-chestxray-dataset

B. PREPROCESSING
Due to the differences in acquisition conditions and patient variability, changes in the overall intensity and contrast are reflected in the different CXRs. The intensity inconsistency of the CXRs may affect the accuracy of the lung field segmentation. Therefore, it is necessary to perform a contrast normalization to ensure the consistency of the CXRs. We adopted contrast limited adaptive histogram equalization [39] to unify the intensity range into [0, 1]. The original spatial resolution of the chest radiographs is high and varied. Thus, we downscaled the original radiographs to a fixed resolution (e.g., 256×256 pixels) for significantly accelerating the implementation of lung field segmentation without compromising the accuracy.

C. TRAINING DETAILS
To improve the performance of our VI-FCN model, a data augmentation strategy [40] was used to augment the training samples. In the training stage of the VI-FCN model, the training datasets were augmented through random flipping, rotation, translation, and zoom. It is worth noting that the augmentation of data was strictly based on clinical facts. For instance, there are cases where the heart is on the right and there are no cases where the head is on the bottom. Thus, only horizontal flip was performed in the augmentation of the data. Considering the different size of thoracic cages of different people, the CXRs were scaled with factors in the range of [0.95, 1.05]. Moreover, to avoid the destabilization of our VI-FCN model, the training datasets were augmented by random rotation (in a range of $[-5, 5]$ degrees) and translation (on a scale of 0.05).

Our proposed VI-FCN model was trained with a batch size of 4 for 100 epochs using an Adam optimizer [41]. The learning rate was set to 10^{-4}. Unless specified, the input size of the VI-FCN was 256×256. Our method was implemented under the framework of PyTorch [42] using a NVIDIA Titan X graphics processing unit (GPU) with 12GB memory. The training of our VI-FCN model took approximately 20 hours. Moreover, the number of parameter and floating point operations (FLOPs) of our VI-FCN are 9.425M and 31.768B, respectively.

In this study, JSRT, the most commonly used public dataset, was used to evaluate the performance of our proposed VI-FCN model. The JSRT dataset is divided into two folds: fold 1 (124 images) and fold 2 (123 images). Two-fold cross-validation was used to divide the training and testing datasets of JSRT. To improve the generalization of the VI-FCN model, datasets, including the CRASS dataset, the MC dataset, the TB dataset, the OpenIST, the Shenzhen dataset, and the Nanfang Hospital dataset, were added into training. Moreover, 35 randomly selected lateral CXRs were used as testing data. Besides, two datasets, including the pediatric CXRs and COVID-19 CXRs without ground true masks, were used to objectively show the generalization ability of the VI-FCN.
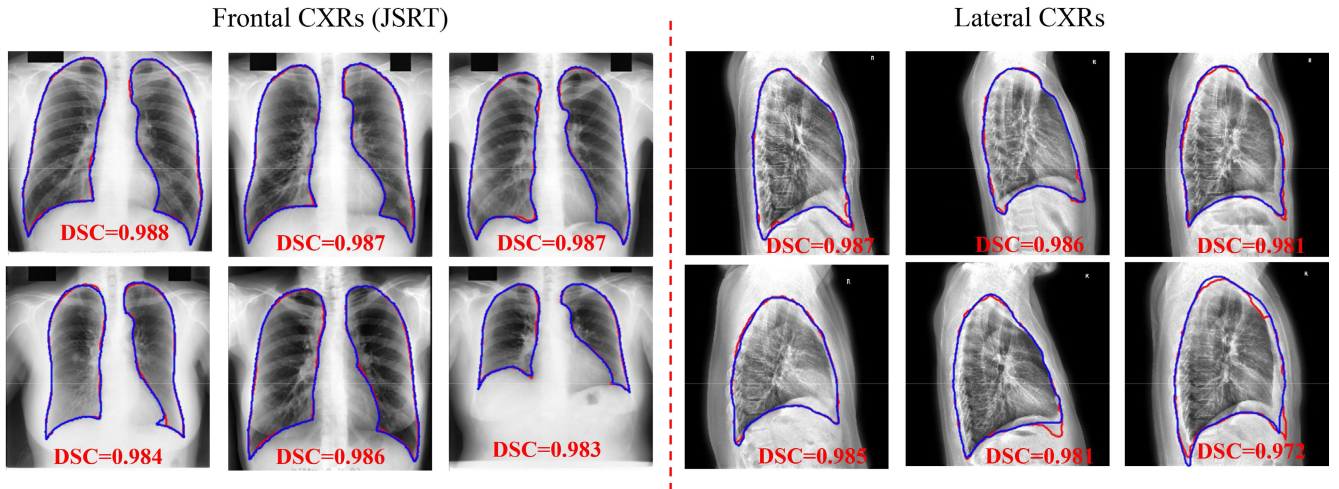
Frontal CXRs (JSRT)   Lateral CXRs

FIGURE 4. Examples of lung field segmentation obtained by VI-FCN on the JSRT dataset (the first and second columns) and our lateral CXRs (the last two columns). Blue and red contours indicate the ground truth and automatic segmentation results, respectively.

D. EVALUATION METRICS

A set of widely used metrics, namely, the Jaccard index (Ω), the Dice similarity coefficient (DSC), and the mean boundary distance (MBD), were performed to evaluate the segmentation performance. The Jaccard index can be formulated as:

$$\Omega = \frac{S \cap T}{S \cup T} \qquad (7)$$

where S is the estimated segmentation mask and T is the ground truth mask. DSC is the overlap ratio between the ground truth mask T and the estimated segmentation mask S:

$$DSC = \frac{2 \times |S \cap T|}{|S| + |T|} \qquad (8)$$

MBD is the average distance between the estimated segmentation boundary S and the ground truth boundary T. Let s_i and t_j be the points on S and T, respectively. The minimum distance of point s_i on S to T was computed as:

$$d(s_i, T) = \min_j \| s_i, t_j \| \qquad (9)$$

For MBD computation, the minimum distance for each point on S to T was calculated, and vice versa. These minimum distances were averaged as MBD:

$$MBD(S, T) = \frac{1}{2}\left(\frac{\sum_i d(s_i, T)}{|\{s_i\}|} + \frac{\sum_j d(t_j, S)}{|\{t_j\}|}\right) \qquad (10)$$

IV. RESULTS

A. OVER PERFORMANCE

Results of segmentation of the lung fields on JSRT dataset and on our lateral CXRs obtained by VI-FCN are shown in Fig. 4. Specifically, VI-FCN achieves mean DSC of 0.979 ± 0.008, mean Ω of 0.959 ± 0.016, and mean MBD of $1.023 \pm 0.487mm$ for the segmentation of lung fields on JSRT dataset. Moreover, VI-FCN achieves mean DSC of 0.973 ± 0.010, mean Ω of 0.947 ± 0.018, and mean
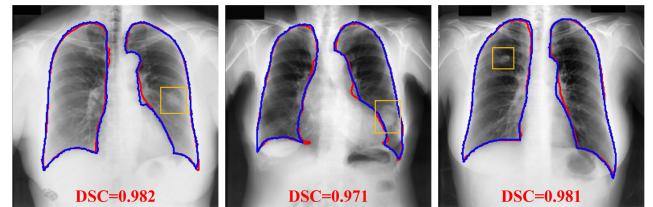

FIGURE 5. Examples of lung field segmentation obtained by VI-FCN on the JSRT dataset with different sizes nodules (indicated by yellow rectangles). Blue and red contours indicate the ground truth and automatic segmentation results, respectively.

TABLE 2. The execution time of the preprocessing, postprocessing, and proposed VI-FCN architectures.

Methods	Preprocessing (CPU)	Postprocessing (CPU)	VI-FCN (CPU)	VI-FCN (GPU)
Time (s)	0.018	0.003	1.387	0.034

MBD of $1.923 \pm 0.755mm$ for the segmentation of lung fields on our lateral CXRs. The JSRT dataset contains CXRs with nodules, thus, we showed the lung field segmentation of CXRs with different sizes nodules in the Fig. 5.

For view identification task, the accuracy is 100% due to significant characteristic differences between frontal and lateral CXR. Table 2 illustrates the execution time of the preprocessing, postprocessing, and proposed VI-FCN architectures for CPU and GPU. The processing time of an image is 0.034s on GPU and 1.387s on CPU. As presented in Table 2, extremely little execution time is taken to segment lung fields, which will be greatly beneficial in large clinical environments. These quantitative results show that the proposed VI-FCN is able to segment the lung fields with superior performance.

B. IMPACT OF λ IN OBJECTIVE FUNCTION

λ is an important parameter in the loss function of our proposed method, which represents the weight between
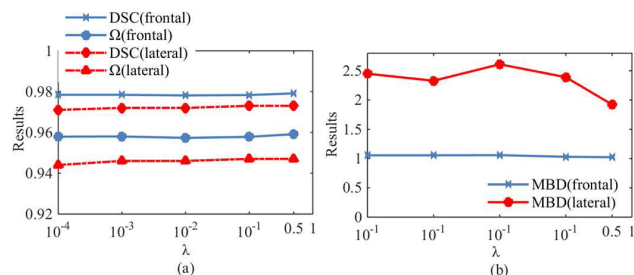
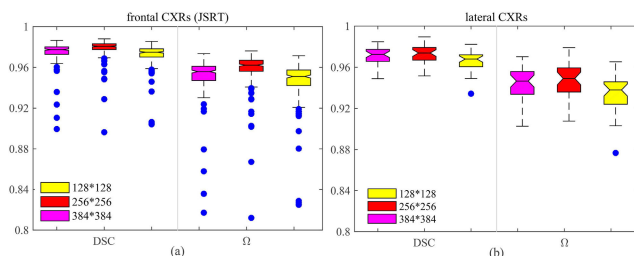**FIGURE 6.** Lung field segmentation performance using various λ.

FIGURE 7. The DSC and Ω results of the segmentation of lung fields on JSRT dataset (a) and our lateral CXRs (b) using the image sizes of 384 × 384, 256 × 256, and 128 × 128 in VI-FCN.

segmentation and classification tasks. Thus, we analyzed the impact of λ by setting the values of 10^{-4}, 10^{-3}, 10^{-2}, 10^{-1} and 0.5. Since the classification task converges easily and quickly, the value of λ has little effect on the final segmentation result. When λ is set to 0.5, although the values of DSC and Ω did not improve significantly, the value of MBD is the lowest (as shown in Fig. 6).

C. OPTIMIZATION OF VI-FCN

Three experiments, including different input sizes of model, different training datasets, and ablation studies, were performed to select the optimal VI-FCN model. Due to that the aforementioned datasets were collected from different centers and under different conditions, the most commonly used strategy was to resize all data into a fixed size. Fig. 7 shows the DSC and Ω results of the segmentation of lung fields on the JSRT dataset and our lateral CXRs using the image sizes of 384 × 384, 256 × 256, and 128 × 128 in VI-FCN. Note that an increase of image size will inevitably increase memory consumption and drag down the execution time. As shown in Fig. 7, the input image size of 256 × 256 achieved the best performance. Considering both the performance of lung fields segmentation and memory consumption, the input size of 256 × 256 is demonstrated to be the most suitable input size for our VI-FCN model.

The diversity of data is a key factor for training a deep learning model. Thus, different training datasets, including balanced data, JSRT dataset, and all data were used to select the optimal VI-FCN model. Specifically, the balanced data denoted that frontal CXRs were randomly chosen the same number of lateral CXRs for each epoch during the training (the ratio of frontal CXRs and lateral CXRs is equal to 1:1).
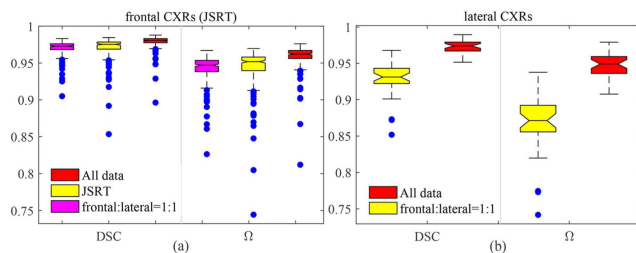

FIGURE 8. The DSC and Ω results of the segmentation of lung fields on JSRT dataset (a) and our lateral CXRs (b) using different datasets to train VI-FCN, including balanced data, JSRT dataset, and all data.

Moreover, there are no lateral CXRs in JSRT dataset. The JSRT dataset was used to train our VI-FCN model for the segmentation of frontal CXRs. The mean DSC and Ω results of using different datasets for training are shown in Fig. 8. Due to the adjusting the ratio of frontal CXRs and lateral CXRs, the total number of CXRs for training decreased. The DSC obtained by using balanced data decreased from 0.979 ± 0.008 (using all data) to 0.971 ± 0.009 for the segmentation of frontal CXRs (JSRT) and decreased from 0.973 ± 0.010 to 0.943 ± 0.017 for the segmentation of lateral CXRs. The VI-FCN achieves the best performance when using all data for training.

The ablation studies were performed to assess the key components of the proposed VI-FCN. The ablation studies include FCN, VI-FCN using only frontal CXRs for training and testing (VI-FCN (frontal)), VI-FCN using only lateral CXRs for training and testing (VI-FCN (lateral)), VI-FCN using only all CXRs for training and testing (VI-FCN (all)), and VI-FCN with post-processing. The results of the ablation studies are listed in Table 3. As illustrated in Table 3 improvements can be achieved in VI-FCN (all) compared with FCN, and slightly improvements can be found in VI-FCN with postprocessing compared with VI-FCN. The details of postprocessing are retaining the two largest connections for frontal CXR, and retaining the largest connection for lateral CXR. To clearly show the importance of postprocessing, Fig. 9 shows partial results of segmentation with false labels of lung fields on JSRT dataset, lateral CXRs and pediatric CXRs using VI-FCN and VI-FCN with postprocessing, respectively. It is worth noting that the results of segmentation of lung fields on pediatric CXRs were obtained by using the VI-FCN (all), and no pediatric CXRs were added to train the VI-FCN. As shown in Fig. 9, due to the high accuracy of VI-FCN on adult CXRs, only a few CXRs have false connections, yet, significant improvements can be found in pediatric CXRs.

D. GENERATION ABILITY OF VI-FCN

The generalization ability is a key factor in training a deep learning model. The performance of segmentation of lung fields is sensitive to the number of CXRs, ground true mask obtained by different radiologists, CXRs from different centers, different types of CXRs (e.g., pediatric CXRs), and lung disease (e.g., COVID-19 CXRs). In order to verify the

TABLE 3. The ablation studies of key components of the proposed VI-FCN, including FCN, VI-FCN (frontal), VI-FCN (lateral), VI-FCN (all), and VI-FCN with postprocessing.

Models	Frontal CXRs (JSRT)			Lateral CXRs		
	DSC	Ω	MBD (*mm*)	DSC	Ω	MBD (*mm*)
FCN	0.975 ± 0.010	0.951 ± 0.018	1.207 ± 0.476	0.971 ± 0.008	0.944 ± 0.015	2.094 ± 0.788
FCN (frontal)	0.974 ± 0.010	0.950 ± 0.018	1.189 ± 0.564	-	-	-
FCN (lateral)	-	-	-	0.967 ± 0.011	0.937 ± 0.021	2.083 ± 0.815
VI-FCN	0.979 ± 0.008	0.959 ± 0.015	1.024 ± 0.488	0.972 ± 0.010	0.947 ± 0.018	1.960 ± 0.777
VI-FCN (postprocessing)	0.979 ± 0.008	0.959 ± 0.016	1.023 ± 0.487	0.973 ± 0.010	0.947 ± 0.018	1.923 ± 0.755

TABLE 4. The performance on JSRT dataset and lateral CXRs obtained bY VI-FCN models, which were trained using 20%, 40%, and 100% of total data.

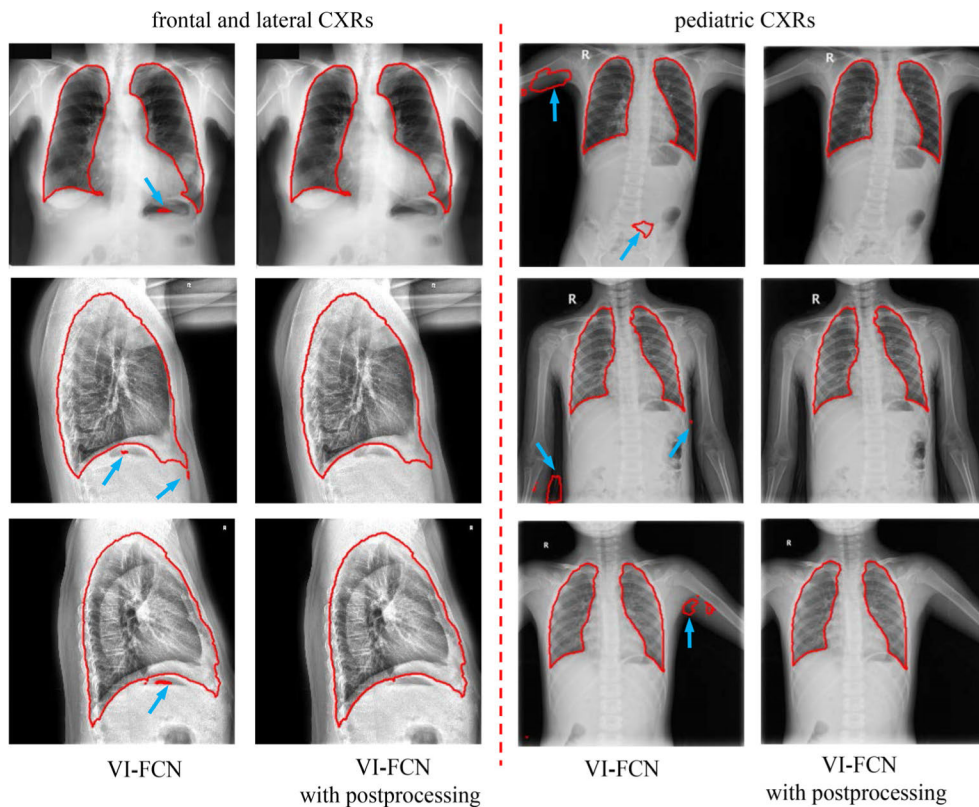| Training data	Frontal CXRs (JSRT)			Lateral CXRs		
	DSC	Ω	MBD (*mm*)	DSC	Ω	MBD (*mm*)
20%	0.976 ± 0.010	0.953 ± 0.019	1.159 ± 0.581	0.957 ± 0.013	0.918 ± 0.024	3.148 ± 1.113
40%	0.977 ± 0.009	0.955 ± 0.016	1.142 ± 0.522	0.969 ± 0.010	0.940 ± 0.018	2.160 ± 0.770
100%	0.979 ± 0.008	0.959 ± 0.016	1.023 ± 0.487	0.973 ± 0.010	0.947 ± 0.018	1.923 ± 0.755

FIGURE 9. Partial results of segmentation with false connections of lung fields on JSRT dataset, lateral CXRs and pediatric CXRs using VI-FCN and VIFCN with post-processing, respectively. Red contours indicate the automatic segmentation results obtained by VI-FCN.

generalization ability of VI-FCN, we randomly selected 20%, 40%, and 100% of total data to train the proposed VI-FCN model and evaluated the performance on JSRT dataset and lateral CXRs, which is illustrated in Table 4. As illustrated in Table 4, when enlarging the dataset, the performance of our VI-FCN gradually improves. Though the improvement is limited (the mean DSC is improved from 0.976 ± 0.010 using

20% of data to 0.979 ± 0.080), large improvement of generalization ability of VI-FCN can be found in segmenting the new types of CXRs (pediatric CXRs) and new lung disease (COVID-19), which are shown in Fig. 10. These results indicate that the proposed VI-FCN has superior generalization ability for segmentation of different types of CXRs and CXRs with new lung diseases.
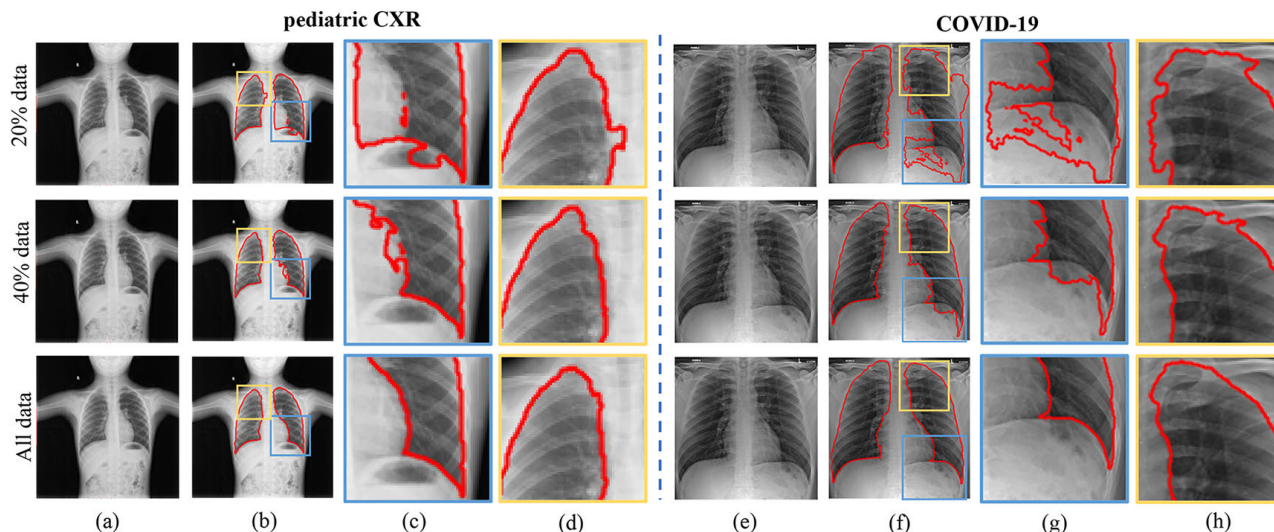
FIGURE 10. Examples of segmentation of lung fields on pediatric CXRs (a-d) and COVID-19 (e-h) by VI-FCN. Red contours indicate the automatic segmentation results obtained by VI-FCN.

TABLE 5. Results of the proposed VI-FCN and current state of-the-art methods for the segmentation of lung fields on JSRT dataset.

Method	DSC	Ω	MBD (*mm*)
Human observer [6]	-	0.946 ± 0.018	1.64 ± 0.69
ASM SIFT [11]	-	0.920 ± 0.031	1.78 ± 0.78
Shape Information Priors [12]	-	0.940 ± 0.053	2.460 ± 2.060
SIFT-Flow [13]	0.967 ± 0.008	0.954 ± 0.015	1.321 ± 0.316
Local SSC [14]	0.972 ± 0.01	0.946 ± 0.019	1.699 ± 0.762
SEDUCM [15]	0.975 ± 0.01	0.952 ± 0.018	1.37 ± 0.67
Encoder-Decoder CNN [25]	0.962 ± 0.008	-	-
Original U-net [26]	0.971	0.944	-
InvertedNet [29]	0.974	0.950	-
FCN [34]	-	0.955 ± 0.015	-
LF-SegNet [43]	-	0.951	-
Variant FCN [44]	-	0.9588	-
CNN with atrous convolutions [27]	0.980 ± 0.008	0.961 ± 0.015	1.237 ± 0.702
VI-FCN	0.979 ± 0.008	0.959 ± 0.016	1.023 ± 0.487

E. COMPARISON WTHE STATE-OF-THE-ART METHODS

Table 5 lists the comparisons between the proposed VI-FCN and the current state-of-the-art methods for the segmentation of lung fields on JSRT dataset. Existing innovative methods include traditional-based methods (Human observer, ASM SIFT, Shape Information Priors, SIFT-Flow, Local SSC, and SEDUCM) and deep learning-based methods (Encoder-Decoder CNN, Original U-net, InvertedNet, FCN, variant FCN, LF-SegNet, and CNN with atrous convolutions). It is clearly that the performance of the proposed VI-FCN significantly surpasses that of the current state-of-the-art methods, except CNN with atrous convolutions. The results of the proposed VI-FCN are slightly worse than CNN with atrous convolutions. However, CNN with atrous convolutions

was ensembled by training three stages of models, which inevitable drags down the execution time. Such a long implementation time is not suitable for large clinical environments.

F. EFFECTIVENES OF VI-FCN ON COVID-19 AND PEDIATRIC CXRs

Under the global pandemic of COVID-19, developing a model of lung field segmentation to analyze CXRs for COVID-19 diagnosis is important. However, due to the emergent attributes of the COVID-19, it is difficult to collect large CXRs of COVID-19 for training a new model. It is of practical significance to use the existing trained model to directly and accurately segment the lung fields. Fig. 11 shows the lung field segmentation of frontal and lateral CXRs using our VIFCN on the COVID-19 CXRs dataset. As shown in Fig. 11, though the intensity in the boundary of lung field is very similar to the surrounding tissue because of the lesion, our VI-FCN can accurately segment the lung fields.

As compared with the adult CXRs, the lung fields occupy a smaller area in the pediatric CXRs, which increase the difficulty in the segmentation task. Although our VI-FCN model was trained with adult CXRs, satisfactory results can be obtained for segmentation of the lung fields on pediatric CXRs, which is shown in Fig. 12. As shown in Fig. 12, though pediatric CXRs are not added in training our VI-FCN model, superior performance can be achieved in segmenting lung fields.

Due to the lack of ground truth in these two datasets, the radiologists classify the results into three levels, including good, acceptable and not acceptable, to evaluate the performance of lung field segmentation. Totally 100 CXRs were randomly selected from pediatric CXRs and COVID-19 CXRs, respectively. The lung field segmentations of 100 pediatric CXRs contain 91 good outcome cases,
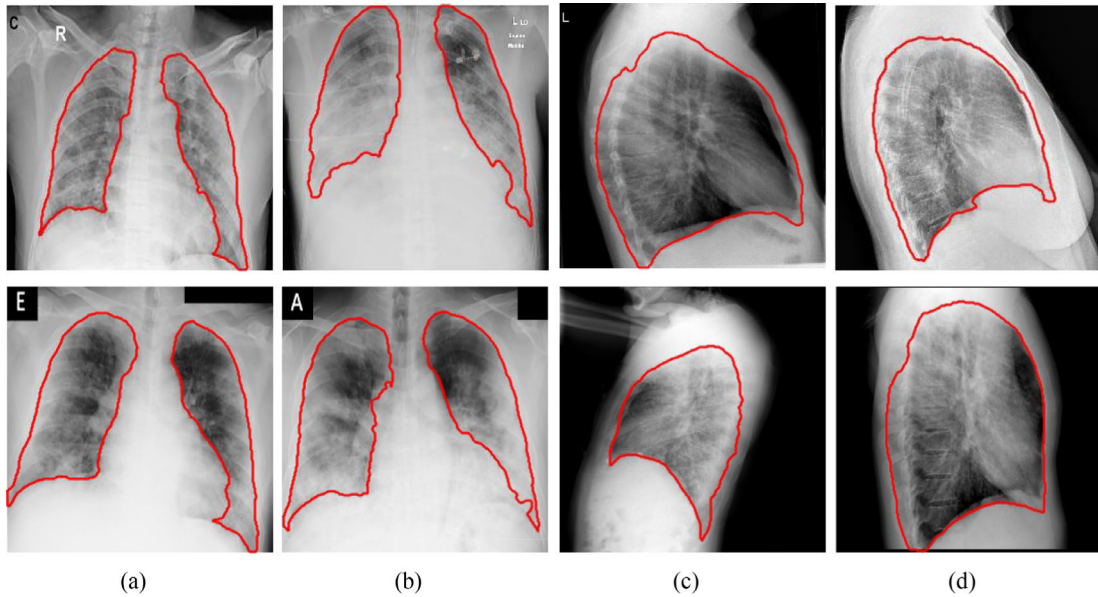
FIGURE 11. Partial results of lung field segmentation of frontal and lateral CXRs on the COVID-19 CXRs dataset. Red contours indicate the automatic segmentation results obtained by VI-FCN.
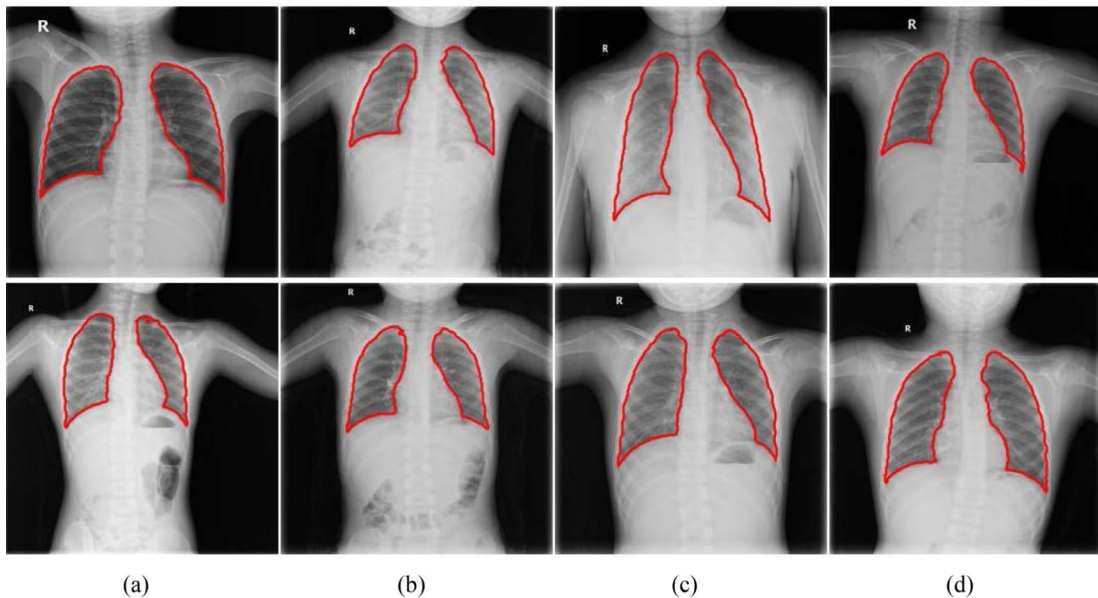

FIGURE 12. Partial results of lung field segmentation of frontal and lateral CXRs on the pediatric CXRs. Red contours indicate the automatic segmentation results obtained by VI-FCN.

8 acceptable outcome cases, and 1 unacceptable outcome case. For the lung field segmentations of 100 COVID-19 CXRs, there are 92 good outcome cases and 8 acceptable outcome cases, which is summarized in Table 6.

V. DISCUSSION

In this study, we proposed an accurate and fast method named VI-FCN for segmenting the lung field of lateral and frontal CXRs and identifying of the lateral and frontal CXRs, simultaneously. Both FCN and VI-FCN use frontal and lateral

CXRs for training, and achieve the frontal and lateral lung field segmentation. The FCN method is used for the lung field segmentation task. Unlike FCN, the proposed VI-FCN is a multi-task learning framework, which contains a lung field segmentation task and a task of classifying frontal and lateral CXRs. Due to the inter-task information exchange and common feature extraction, the multi-task learning outperforms the approaches that address each task individually [45]. Moreover, as illustrated in Table 3, the performance of the proposed VI-FCN is better than that of FCN. Segmentation

TABLE 6. Radiologist evaluation on pediatric and COVID-19 CXRs.

	Good	Acceptable	Not acceptable	Total
Pediatric CXRs	91	8	1	100
COVID-19 CXRs	92	8	0	100

of both frontal and lateral CXRs simultaneously can benefit clinical diagnosis of cardiothoracic and lung diseases [48]. And in actual clinical, the view (frontal or lateral view) of CXR is manually registered in DICOM format, which will inevitably cause incorrect annotations. Automated view identification ensures automatic classification of CXR views, which can help develop an end-to-end automatic analysis the model of lung diseases without manual classification. However, only a few deep learning-based studies have been reported for lung field segmentation in CXRs. None of these studies have been developed for lung field segmentation on lateral CXRs. Only in the early days, a few classic-based methods [46], [47] focus on lung field segmentation on both frontal and lateral CXRs. However, these methods can only achieve segmenting the lung field on frontal and lateral CXRs separately. Both the accuracy of lung field segmentation and the long execution time are unacceptable in large clinical environments.

As illustrated in Table 3, almost no improvement is found between VI-FCN and VI-FCN with postprocessing. Due to the high accuracy of adult lung field segmentation using the proposed VI-FCN, only a few subjects have false connection of the segmentation. For practical application, the results obtained by the VI-FCN are sufficient in terms of speed. By contrast, the use of the VI-FCN with post-processing to further refine the segmentation is suitable in terms of precision. As compared with the adult CXRs, the lung field in the pediatric CXRs occupies a smaller area, the post-processing step is more important for segmenting the lung field on untrained pediatric CXRs (as shown in Fig. 9).

As illustrated in Table 5, the results of CNN with atrous convolutions [24] are slightly better than the proposed VI-FCN. However, CNN with atrous convolutions is ensembled by training three stages of models which inevitable drags down the execution time. The longtime of implementation is not suitable in large clinical environments. It has been reported that the fastest implementation of a model for lung field segmentation on GPU is 0.03s [23]. The execution time of our VI-FCN on GPU is also 0.03s, which means that our VI-FCN has great applicability in large clinical environments.

Due to the global pandemic of COVID-19, medical resources become insufficient in many regions. The segmentation of lung fields is a key step in the training of classification model. It is difficult to collect a large number of COVID-19 CXRs with ground true mask. Thus, the generalization ability of existing models becomes very important. As shown in Fig. 11-12 superior results can be obtained by directly using our VI-FCN model for lung field segmentation

Downsampling Path	
Input, m=1	
3×3 Convolution, m=48	
DB (4 layers) +TD, m=112	
DB (5 layers) +TD, m=192	
DB (7 layers) +TD, m=304	
DB (10 layers) +TD, m=464	
DB (12 layers) +TD, m=656	
Upsampling Path	**Auxiliary Path**
DB (15 layers), m=896	2×2 Max pooling
TU+DB (12 layers), m=1088	3×3 Convolution
TU+DB (10 layers), m=816	linear layer, m=1
TU+DB (7 layers), m=578	
TU+DB (5 layers), m=384	
TU+DB (4 layers), m=256	
1×1 Convolution, m=1	

FIGURE 13. The architecture of VI-FCN.

layer	Transition Down (TD)	Transition Up (TU)
Batch Normalization	Batch Normalization	3×3 Transposed Convolution *stride*=2
ReLU	ReLU	
3×3 Convolution	1×1 Convolution	
Dropout *p*=0.2	Dropout *p*=0.2	
	2×2 Max pooling	

FIGURE 14. The details of the layer of BD, TD and TU.

on COVID-19 CXRs and pediatric CXRs. As noted in the first column of Fig. 9, several lung field segmentation with false connections are also shown for more comprehensively presenting the performance of VI-FCN. The accuracy of the proposed VI-FCN for lung field segmentation on COVID-19 CXRs and pediatric CXRs needs to be evaluated in the future when medical resources are not so scarce.

In the future, we will use the evaluation metrics to accurately evaluate the generalization ability of the proposed VI-FCN on COVID-19 CXRs and pediatric CXRs. Moreover, we will develop a classification model using the segmented lung field for COVID-19 diagnosis.

VI. CONCLUSION

In this study, we have proposed an accurate and fast method, named VI-FCN, for simultaneously segmenting the lung field of lateral and frontal CXRs and simultaneously classifying the lateral and frontal CXRs. The FCN branch was developed to simultaneously segment the lung fields of lateral and frontal CXRs, and the VI branch was used to correct the incorrect annotations in DICOM images and boost the performance of lung field segmentation. To enhance the generalization ability of the proposed VI-FCN, large amounts of data from different centers and different conditions were added into training. The proposed VI-FCN achieved superior results of lung field segmentation on untrained COVID-19 and pediatric CXRs. Moreover, the proposed VI-FCN can

achieve competitive performance and less computation time than several state-of-the-art methods.

ACKNOWLEDGMENT

(Yuhua Xi and Liming Zhong contributed equally to this work.)

APPENDIX
A. DETAILS OF THE VI-FCN

As shown in Fig. 13 and Fig. 14, we summary details of VI-FCN, and define the dense block layer, TD and TU. The dense block is composed of some layers, which the growth rate of layers is set to 16. As already described in method, each layer includes BN, followed by ReLU, a 3×3 convolution and dropout with probability $p = 0.2$. TD is composed of BN, followed by ReLU, a 1×1 convolution, dropout with $p = 0.2$ and a 2×2 max pooling. For TU, it is a 3×3 transposed convolution with stride of 2 for upsampling. VI-FCN contains two branches: FCN branch and VI branch. The downsampling path is shared by FCN and VI branch.

ETHICS APPROVAL AND CONSENT TO PARTICIPATE

This work was approved by the institutional review board, the need for informed patient consent for inclusion was waived.

REFERENCES

[1] S. Raoof, D. Feigin, A. Sung, S. Raoof, L. Irugulpati, and E. C. Rosenow, III, "Interpretation of plain chest roentgenogram," *Chest*, vol. 141, no. 2, pp. 545–558, Feb. 2012.

[2] R. Dhoot, J. M. Humphrey, P. O'Meara, A. Gardner, C. J. McDonald, K. Ogot, S. Antani, J. Abuya, and M. Kohli, "Implementing a mobile diagnostic unit to increase access to imaging and laboratory services in western kenya," *BMJ Global Health*, vol. 3, no. 5, Oct. 2018, Art. no. e000947.

[3] B. van Ginneken and B. M. T. H. Romeny, "Automatic segmentation of lung fields in chest radiographs," *Med. Phys.*, vol. 27, no. 10, pp. 2445–2455, Oct. 2000.

[4] M. S. Brown, L. S. Wilson, B. D. Doust, R. W. Gill, and C. Sun, "Knowledge-based method for segmentation and analysis of lung boundaries in chest X-ray images," *Comput. Med. Imag. Graph.*, vol. 22, no. 6, pp. 463–477, Nov. 1998.

[5] J. Duryea and J. M. Boone, "A fully automated algorithm for the segmentation of lung fields on digital chest radiographic images," *Med. Phys.*, vol. 22, no. 2, pp. 183–191, Feb. 1995.

[6] B. van Ginneken, M. B. Stegmann, and M. Loog, "Segmentation of anatomical structures in chest radiographs using supervised methods: A comparative study on a public database," *Med. Image Anal.*, vol. 10, no. 1, pp. 19–40, Feb. 2006.

[7] M. F. McNitt-Gray, H. K. Huang, and J. W. Sayre, "Feature selection in the pattern classification problem of digital chest radiograph segmentation," *IEEE Trans. Med. Imag.*, vol. 14, no. 3, pp. 537–547, Sep. 1995.

[8] W. S. H. M. W. Ahmad, W. M. D. W Zaki, and M. F. A. Fauzi, "Lung segmentation on standard and mobile chest radiographs using oriented Gaussian derivatives filter," *Biomed. Eng. OnLine*, vol. 14, no. 1, p. 20, Dec. 2015.

[9] S. Juhász, Á. Horváth, L. Nikházy, and G. Horváth, "Segmentation of anatomical structures on chest radiographs," in *Proc. 12th Medit. Conf. Med. Biol. Eng. Comput. (MEDICON)*, 2010, pp. 359–362.

[10] P. Annangi, S. Thiruvenkadam, A. Raja, H. Xu, X. Sun, and L. Mao, "A region based active contour method for X-ray lung segmentation using prior shape and low level features," in *Proc. IEEE Int. Symp. Biomed. Imag., From Nano Macro (ISBI)*, Apr. 2010, pp. 892–895.

[11] Y. Shi, F. Qi, Z. Xue, L. Chen, K. Ito, H. Matsuo, and D. Shen, "Segmenting lung fields in serial chest radiographs using both population-based and patient-specific shape statistics," *IEEE Trans. Med. Imag.*, vol. 27, no. 4, pp. 481–494, Apr. 2008.

[12] A. Dawoud, "Lung segmentation in chest radiographs by fusing shape information in iterative thresholding," *IET Comput. Vis.*, vol. 5, no. 3, pp. 185–190, May 2011.

[13] S. Candemir, S. Jaeger, K. Palaniappan, J. P. Musco, R. K. Singh, Z. Xue, A. Karargyris, S. Antani, G. Thoma, and C. J. McDonald, "Lung segmentation in chest radiographs using anatomical atlases with nonrigid registration," *IEEE Trans. Med. Imag.*, vol. 33, no. 2, pp. 577–590, Feb. 2014.

[14] Y. Shao, Y. Gao, Y. Guo, Y. Shi, X. Yang, and D. Shen, "Hierarchical lung field segmentation with joint shape and appearance sparse learning," *IEEE Trans. Med. Imag.*, vol. 33, no. 9, pp. 1761–1780, Sep. 2014.

[15] W. Yang, Y. Liu, L. Lin, Z. Yun, Z. Lu, Q. Feng, and W. Chen, "Lung field segmentation in chest radiographs from boundary maps by a structured edge detector," *IEEE J. Biomed. Health Informat.*, vol. 22, no. 3, pp. 842–851, May 2018.

[16] M. De Bruijne and M. Nielsen, "Shape particle filtering for image segmentation," in *Proc. Int. Conf. Med. Image Comput. Comput.-Assist. Intervent. (MICCAI)*, 2004, pp. 168–175.

[17] T. F. Cootes, C. J. Taylor, D. H. Cooper, and J. Graham, "Active shape models-their training and application," *Comput. Vis. Image Understand.*, vol. 61, no. 1, pp. 38–59, Jan. 1995.

[18] T. F. Cootes, G. J. Edwards, and C. J. Taylor, "Active appearance models," *IEEE Trans. Pattern Anal. Mach. Intell.*, vol. 23, no. 6, pp. 681–685, Jun. 2001.

[19] T. Xu, M. Mandal, R. Long, I. Cheng, and A. Basu, "An edge-region force guided active shape approach for automatic lung field detection in chest radiographs," *Comput. Med. Imag. Graph.*, vol. 36, no. 6, pp. 452–463, Sep. 2012.

[20] T. Peng, Y. Wang, T. C. Xu, and X. Chen, "Segmentation of lung in chest radiographs using hull and closed polygonal line method," *IEEE Access*, vol. 7, pp. 137794–137810, 2019.

[21] T. Peng, T. C. Xu, Y. Wang, and F. Li, "Deep belief network and closed polygonal line for lung segmentation in chest radiographs," *Comput. J.*, Dec. 2020. [Online]. Available: https://academic.oup.com/comjnl/advance-article-abstract/doi/10.1093/comjnl/bxaa148/6029261, doi: 10.1093/comjnl/bxaa148.

[22] D. Hong, L. Gao, J. Yao, B. Zhang, A. Plaza, and J. Chanussot, "Graph convolutional networks for hyperspectral image classification," *IEEE Trans. Geosci. Remote Sens.*, early access, Aug. 18, 2020, doi: 10.1109/TGRS.2020.3015157.

[23] D. Hong, L. Gao, N. Yokoya, J. Yao, J. Chanussot, Q. Du, and B. Zhang, "More diverse means better: Multimodal deep learning meets remote-sensing imagery classification," *IEEE Trans. Geosci. Remote Sens.*, early access, Aug. 24, 2020, doi: 10.1109/TGRS.2020.3016820.

[24] S. Candemir and S. Antani, "A review on lung boundary detection in chest X-rays," *Int. J. Comput. Assist. Radiol. Surg.*, vol. 14, no. 4, pp. 563–576, Apr. 2019.

[25] A. Kalinovsky and V. Kovalev, "Lung image segmentation using deep learning methods and convolutional neural networks," in *Proc. Pattern Recgnit. Inf. Process.* Minsk, Belarus: Publishing Center of BSU, 2016, pp. 21–24.

[26] O. Ronneberger, P. Fischer, and T. Brox, "U-Net: Convolutional networks for biomedical image segmentation," in *Proc. Int. Conf. Med. Image Comput. Comput.-Assist. Intervent. (MICCAI)*, 2015, pp. 234–241.

[27] S. Hwang and S. Park, "Accurate lung segmentation via network-wise training of convolutional networks," in *Deep Learning in Medical Image Analysis and Multimodal Learning for Clinical Decision Support.* Québec City, QC, Canada, 2017, pp. 92–99.

[28] B. N. Narayanan and R. C. Hardie, "A computationally efficient U-Net architecture for lung segmentation in chest radiographs," in *Proc. IEEE Nat. Aerosp. Electron. Conf. (NAECON)*, Jul. 2019, pp. 279–284.

[29] A. A. Novikov, D. Lenis, D. Major, J. Hladuvka, M. Wimmer, and K. Buhler, "Fully convolutional architectures for multiclass segmentation in chest radiographs," *IEEE Trans. Med. Imag.*, vol. 37, no. 8, pp. 1865–1876, Aug. 2018.

[30] R. Hooda, A. Mittal, and S. Sofat, "Lung segmentation in chest radiographs using fully convolutional networks," *TURKISH J. Electr. Eng. Comput. Sci.*, vol. 27, no. 2, pp. 710–722, Jan. 2019.

[31] A. Singh, B. Lall, B. K. Panigrahi, A. Agrawal, A. Agrawal, D. Christopher, and B. Thangakunam, "Deep LF-Net: Semantic lung segmentation from Indian chest radiographs including severely unhealthy images," 2020, *arXiv:2011.09695*. [Online]. Available: http://arxiv.org/abs/2011.09695

[32] W. Dai, N. Dong, Z. Wang, X. Liang, H. Zhang, and E. P. Xing, "Scan: Structure correcting adversarial network for organ segmentation in chest X-rays," in *Deep Learning in Medical Image Analysis and Multimodal Learning for Clinical Decision Support*. Granada, Spain, 2018, pp. 263–273.

[33] J. Shiraishi, S. Katsuragawa, J. Ikezoe, T. Matsumoto, T. Kobayashi, K.-I. Komatsu, M. Matsui, H. Fujita, Y. Kodera, and K. Doi, "Development of a digital image database for chest radiographs with and without a lung nodule: Receiver operating characteristic analysis of radiologists' detection of pulmonary nodules," *Amer. J. Roentgenol.*, vol. 174, no. 1, pp. 71–74, Jan. 2000.

[34] Y. Oh, S. Park, and J. C. Ye, "Deep learning COVID-19 features on CXR using limited training data sets," *IEEE Trans. Med. Imag.*, vol. 39, no. 8, pp. 2688–2700, Aug. 2020.

[35] S. Jégou, M. Drozdzal, D. Vazquez, A. Romero, and Y. Bengio, "The one hundred layers tiramisu: Fully convolutional DenseNets for semantic segmentation," in *Proc. IEEE Conf. Comput. Vis. Pattern Recognit. Workshops (CVPRW)*, Jul. 2017, pp. 11–19.

[36] C.-F. Yeh et al., "A cascaded learning strategy for robust COVID-19 pneumonia chest X-ray screening," 2020, *arXiv:2004.12786*. [Online]. Available: http://arxiv.org/abs/2004.12786

[37] S. Ioffe and C. Szegedy, "Batch normalization: Accelerating deep network training by reducing internal covariate shift," 2015, *arXiv:1502.03167*. [Online]. Available: http://arxiv.org/abs/1502.03167

[38] B. Xu, N. Wang, T. Chen, and M. Li, "Empirical evaluation of rectified activations in convolutional network," 2015, *arXiv:1505.00853*. [Online]. Available: http://arxiv.org/abs/1505.00853

[39] A. M. Reza, "Realization of the contrast limited adaptive histogram equalization (CLAHE) for real-time image enhancement," *J. VLSI Signal Process.-Syst. Signal, Image, Video Technol.*, vol. 38, no. 1, pp. 35–44, Aug. 2004.

[40] Z. Zhong, L. Zheng, G. Kang, S. Li, and Y. Yang, "Random erasing data augmentation," in *Proc. Conf. AAAI Artif. Intell.*, 2020, pp. 13001–13008.

[41] D. P. Kingma and J. Ba, "Adam: A method for stochastic optimization," 2014, *arXiv:1412.6980*. [Online]. Available: http://arxiv.org/abs/1412.6980

[42] P. Adam, G. Sam, C. Soumith, C. Gregory, Y. Edward, D. Zachary, L. Zeming, D. Alban, A. Luca, and L. Adam, "Automatic differentiation in pytorch," in *Proc. Neural Inf. Process. Syst.*, 2017, pp. 1–4.

[43] A. Mittal, R. Hooda, and S. Sofat, "LF-SegNet: A fully convolutional encoder–decoder network for segmenting lung fields from chest radiographs," *Wireless Pers. Commun.*, vol. 101, no. 1, pp. 511–529, Jul. 2018.

[44] R. Hooda, A. Mittal, and S. Sofat, "An efficient variant of fully-convolutional network for segmenting lung fields from chest radiographs," *Wireless Pers. Commun.*, vol. 101, no. 3, pp. 1559–1579, Aug. 2018.

[45] Z. Xu, Y. Huo, J. Park, B. Landman, A. Milkowski, S. Grbic, and S. Zhou, "Less is more: Simultaneous view classification and landmark detection for abdominal ultrasound images," in *Proc. Int. Conf. Med. Image Comput. Comput.-Assist. Intervent. (MICCAI)*, 2018, pp. 711–719.

[46] S. G. Armato, III, "Automated lung segmentation in digital posteroanterior and lateral chest radiographs: Applications in diagnostic radiology and nuclear medicine," *Med. Phys.*, vol. 24, no. 12, p. 2056, 1997.

[47] S. G. Armato, III, M. L. Giger, K. Ashizawa, and H. Macmahon, "Automated lung segmentation in digital lateral chest radiographs," *Med. Phys.*, vol. 25, no. 8, pp. 1507–1520, Aug. 1998.

[48] Y. Gordienko, P. Gang, J. Hui, W. Zeng, Y. Kochura, O. Alienin, O. Rokovyi, and S. Stirenko, "Deep learning with lung segmentation and bone shadow exclusion techniques for chest X-ray analysis of lung cancer," in *Proc. Int. Conf. Comput. Sci. Eng. Educ. Appl. (CCSEA)*, 2018, pp. 638–647.

LIMING ZHONG received the B.S. and Ph.D. degrees from the Department of Biomedical Engineering, Southern Medical University, Guangzhou, China, in 2013 and 2019, respectively. Her research interests include medical image analysis, machine learning, deep learning, computerized-aid diagnosis, and medical image reconstruction.

WEIJIE XIE is currently pursuing the master's degree with the Department of Biomedical Engineering, Southern Medical University, Guangzhou, China. His research interests include medical image analysis, machine learning, deep learning, and computerized-aid diagnosis.

GENGGENG QIN received the B.Sc. degree in medicine from Sun Yat-sen University, Guangzhou, China, in 2007, and the M.Sc. degree in medical imageology from Southern Medical University, Guangzhou, in 2014. He is currently an Associate Chief Physician with the Department of Radiology, Nanfang Hospital, Southern Medical University. He is also a Visiting Scholar with the Department of Radiation Oncology, University of Texas Southwestern Medical Center, Dallas, TX, USA. He has published 26 journal articles. His current research interests include radiomics, medical image analysis, deep learning, machine learning, and artificial intelligence.
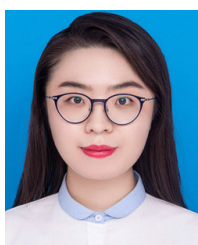
YUNBI LIU was born in China, in 1994. She received the bachelor's degree in biomedical engineering from Southern Medical University, Guangzhou, China, in 2015, where she is currently pursuing the Ph.D. degree with the Department of Biomedical Engineering. Her research interests include medical image analysis and computerized-aid diagnosis.

QIANJIN FENG (Member, IEEE) received the M.S. and Ph.D. degrees in biomedical engineering from First Military Medical University, China, in 2000 and 2003, respectively. From 2003 to 2004, he was a Faculty Member with the School of Biomedical Engineering, First Military Medical University. Since 2004, he has been with Southern Medical University, China, where he is currently a Professor and the Dean of the School of Biomedical Engineering. His research interests include medical image analysis, pattern recognition, and computerized-aided diagnosis.

WEI YANG received the B.Sc. degree in automation from the Wuhan University of Science and Technology, Wuhan, China, in 2001, the M.Sc. degree in control theory and control engineering from Xiamen University, Xiamen, China, in 2005, and the Ph.D. degree in biomedical engineering from Shanghai Jiao Tong University, Shanghai, China, in 2009. He is currently a Professor with the School of Biomedical Engineering, Southern Medical University, Guangzhou, China. His research interests include medical image analysis, machine learning, and computerized-aid diagnosis.

YUHUA XI received the bachelor's degree in biomedical engineering from Southern Medical University, Guangzhou, China, in 2018, where she is currently pursuing the master's degree in engineering with the Department of Biomedical Engineering. Her researches focus on the segmentation of medical images and bone suppression in CXRs.

• • •